CrossMark

Elastic vortices and thermally-driven cracks in brittle materials with peridynamics

**Zhanping Xu · Guanfeng Zhang ·
Ziguang Chen · Florin Bobaru**

Abstract Instabilities in thermally-driven crack growth in thin glass plates have been observed in experiments that slowly immerse a hot, pre-notched glass slide into a cold bath. We show that a nonlocal model of thermomechanical brittle fracture with minimal input parameters can predict the entire phase diagram of fracture measured in experiments for the low immersion speed regime. Geometrical restrictions to crack growth commonly found in other approaches are absent here. We discuss a method for determining the appropriate size of the peridynamic horizon based on a data point around a separating line between crack-type zones in the experimental phase diagram. Once the nonlocal size is smaller than the length-scale introduced by the thermal gradient, the computational results show that no fracture criterion is needed beyond Griffith's criterion to capture the observed instabilities. The combination of thermal gradients and competing contraction forces on the two sides of the crack are behind the observed crack path instabilities. Elastic (velocity) vortices of material points show how and why the cracks develop along the observed paths. Our results demonstrate that thermally-driven fracture in brittle materials can be predicted with accuracy. We anticipate that this model will lead to design protocols for controlled fracture in brittle materials relevant in materials science and advanced manufacturing.

Keywords Peridynamics · Crack growth · Thermally-driven cracks · Thermoelasticity · Elastic vortices · Quenched glass

Z. Xu · G. Zhang · F. Bobaru (✉)
Department of Mechanical and Materials Engineering, University of Nebraska-Lincoln, Lincoln, NE 68588, USA
e-mail: fbobaru2@unl.edu

Z. Chen
Department of Mechanics, Huazhong University of Science and Technology, Wuhan 430074, China

1 Introduction

When a thin glass plate seeded with an edge crack is slowly pushed from an oven into cold water, an interesting transition between no crack growth, straight crack, oscillating crack, or branched crack happens. Three main parameters determine the behavior: the plate's immersion velocity, the plate's width, and the temperature gap between the oven and water bath (Yuse and Sano 1993, 1997). When the crack propagates, its propagation speed is close to the plate velocity (< 50 mm/s), which is six orders of magnitude lower than the Rayleigh wave speed (km/s). Therefore, this fracture process in glass can be considered as quasi-static and should be distinguished from the dynamic fracture in glass (e.g. Hu et al. 2013). The experimental setup used by Ronsin et al. (1995) and Ronsin and Perrin (1998) allowed the authors to explore the very

low plate velocity regime in detail and study the effect the plate width on the fracture process. They found non-linear transition curves between the no crack, straight crack, and oscillatory crack regimes in a phase-diagram of plate width versus plate velocity. Yang and Ravi-Chandar (2001) redesigned the experimental setup to allow open observations of the crack growth. These experiments were performed on slightly thicker glass (0.9 mm thick glass slides) which could be responsible for the apparent 3D effects (cracks tilting through the thickness) and unstable crack growth. The authors of Yang and Ravi-Chandar (2001) found that the T-stress criterion of Cotterell and Rice (1980) is not applicable in this situation, noticing that the transition from a straight to an oscillatory crack path does not coincide with the location at which the T-stress becomes positive. Sakaue et al. (2008) also found that the T-stress criterion is inappropriate to evaluate the crack path instability in a quenched thin glass plate. Yoneyama et al. (2008), Yoneyama and Sakaue (2014) applied an experimental-numerical hybrid method to analyze the stress field around the oscillating the crack tip. They showed that mode-II stress intensity factor K_{II} is non-zero even though the crack propagates smoothly.

Analytical studies for predicting the observed behavior in quenched glass have focused on the transition from the straight crack growth to oscillating crack. Marder (1994) calculated the conditions under which this first bifurcation occurs using T-stress criterion. This criterion was later found, via experimental investigations, to fail to predict the oscillatory instability (Ronsin and Perrin 1998; Yang and Ravi-Chandar 2001; Sakaue et al. 2008).

Various computational models were employed to simulate thermally-driven crack growth in thin glass plates. Some models considered the problem as a dynamic fracture problem, see for example, treatments using the cohesive element method (Ferney et al. 1999), the Extended Finite Element Method (XFEM) (Menouillard and Belytschko 2011), the boundary element method (Yang and Ravi-Chandar 2001), and Peridynamics (Kilic and Madenci 2009). While some of the behavior seen in experiments was partially reproduced in these simulations (e.g., oscillating cracks), in some instances unphysical parameters (e.g., unrealistically fast immersion speeds, temperatures beyond the glass melting point, etc.) had to be used due to the small time steps required by the explicit dynamic solution methods (Ferney et al. 1999; Kilic and Madenci 2009;

Menouillard and Belytschko 2011). Quasi-static fracture models were also used to predict the oscillating cracks observed in experiments, including the spring model (Hayakawa 1994), the phase field method (Corson et al. 2009), and energy minimization via variational formulation (Bourdin 2007). However, all such studies were either purely qualitative or were using unphysical parameters to manage to reproduce, partially, some of the characteristics of the observed phenomenon.

Corson et al. (2009) obtained smooth oscillating crack path in their phase field simulation by applying the principle of local symmetry (PLS) and the Griffith criterion. However, their results are only qualitative (scaled units and analytical thermal field were used) and some details on the transition curves are not reproduced.

In the present work, we introduce a peridynamic model that can predict the entire spectrum of physical behavior for thermally-driven fracture in a thin glass plate for the experimental conditions of low plate immersion speed region (0.05–0.5 mm/s). Here we focus on this particular range of immersion velocities for the following reasons:

(a) Our intention is to use experimentally measured Our intention is to use experimentally measured temperatures, and these temperature fields are provided in the literature only for immersion speeds $v = 0.05, 0.3$, and 0.5 mm/s (see Ronsin et al. 1995).

(b) At these immersion speeds, for sufficiently thin specimens, the 3D effects are negligible since the plate thickness does not play a role in the heat flow problem and a 1D approximate representation of the thermal field is sufficient.

The set of material parameters used by the model is minimal: thermo-elastic data, and fracture energy of glass. We find that under the special type of very small and transient thermal strains, the discrete peridynamic model can leave unbroken bonds bridging a crack. This leads to configurations that cannot sustain a constantly undulating crack path. Experiments show that undulating cracks with almost constant wavelength and amplitude are common in this type of conditions.

To correct this deficiency caused by utilizing a bond-failure criterion exclusively based on critical tensile strain in a bond, we introduce a new and simple addi-

tion to it that does not require tracking of the crack path and ensures that even for small shear no bonds bridging the crack are left behind.

The different fracture behaviors (no-crack, straightly propagating crack, oscillating crack, and branching cracks) are autonomous outcomes of applying only a critical bond stretch criterion (equivalent to Griffith criterion in classical fracture mechanics) together with the proposed correction. No other failure criteria (e.g. PLS) or any dynamic assumptions of crack path development are required. We solve the problem as quasi-static peridynamic with a static solver based on the nonlinear conjugate gradient (NCG) method (Shewchuk 1994). Using the actual physical parameters from experiments, we reproduce the detailed phase diagram that delimitates the crack patterns in terms of immersion speed and plate width. The wavelengths of the oscillating cracks and the location of the crack tip relative to the oven entrance agree remarkably well with the experimental results. Finally, to enhance the efficiency of the peridynamic computations, we use GPU-based algorithms for the NCG solvers of the quasi-static equations.

The paper is organized as follows: Sect. 2 presents a brief introduction of the peridynamic model. Section 3 describes our simulation setup for the quenched glass experiment. Section 4 presents our numerical results and discussion. We summarize our results in Sect. 5.

2 The peridynamic model

The bond-based peridynamic theory is adequate to describe the fracture in soda-lime glass, which, for the temperature range considered in the experiments from room temperature up to 300 °C, can be taken as a linear-elastic and brittle material. The details of the model for dynamic fracture and numerical implementation can be found in Bobaru and Zhang (2015). The effect of the fracture on the thermal field can be ignored for the thin glass plate in the experimental conditions and a one-way coupled thermal-mechanical model is adequate for the low immersion speed tests discussed here. We summarize the thermo-mechanical model (Kilic and Madenci 2010) below and focus on the implementation of the static solver using the conjugate gradient method.

The equation of motion of any node at x in the reference configuration at time t is given by (Kilic and Madenci 2010):

$$\rho \ddot{u}\left(x, t\right) = \int_{\mathcal{H}_x} f\left(\hat{x} - x, u\left(\hat{x}, t\right) - u\left(x, t\right), T_{avg}\right)$$
$$\mathrm{d}V_{\hat{x}} + b\left(x, t\right), \quad (1)$$

where ρ is the mass density, u is the displacement vector field, $T_{\mathrm{avg}} = \left(T\left(\hat{x}, t\right) + T\left(x, t\right)\right)/2$ is the average thermal field, H_x is the neighborhood region of x (called the horizon region), f is the pair-wise force function, and b is the prescribed body force density field.

For a static problem, left side of Eq. 1 vanishes, which leads to

$$\int_{\mathcal{H}_x} f\left(\hat{x} - x, u\left(\hat{x}\right) - u\left(x\right), T_{\mathrm{avg}}\right) \mathrm{d}V_{\hat{x}} + b\left(x\right) = 0, \quad (2)$$

for every node x. Here we denote $\xi = \hat{x} - x$ as the relative reference position between node x and $\hat{x}$, $\eta = u\left(\hat{x}, t\right) - u\left(x, t\right)$ as the relative displacement, average temperature T_{avg} as T for convenience, and $\xi + \eta = \hat{y} - y$ represents the current relative position between the nodes. The interaction between material points is set to zero beyond a certain horizon size δ, such that

$$f\left(\xi, \eta, T\right) = 0 \quad \text{if} \quad |\xi| > \delta. \quad (3)$$

The force density function is given as

$$f\left(\xi, \eta, T\right) = f\left(|\xi + \eta|, |\xi|, T\right) \frac{\xi + \eta}{|\xi + \eta|}, \quad (4)$$

where f is a scalar-valued function of the distance between the nodes in reference and deformed configurations. In this work, we use a Prototype Microelastic Brittle (PMB) material model (Silling and Askari 2005), in which f is defined as

$$f\left(|\xi + \eta|, |\xi|, T\right) = g\left(s\left(\xi, \eta\right), T\right) h\left(\xi, \eta, T\right), \quad (5)$$

where

$$s = \frac{|\xi + \eta| - |\xi|}{|\xi|} = \frac{|\hat{y} - y| - |\hat{x} - x|}{|\hat{x} - x|}, \quad (6)$$

is the bond stretch, and g is a linear scalar-valued function given by

$$g\left(s, T\right) = \begin{cases} c\left(1 - \frac{|\xi|}{\delta}\right)\left(s - \alpha_T T\right) & \text{if} \quad |\xi| < \delta, \\ 0 & \text{otherwise,} \end{cases} \quad (7)$$

where α_T is linear thermal expansion coefficient, and c is the spring constant in the form of

$$c = \frac{36E}{\pi \delta^3} \quad (8)$$

for conical micromodulus function in 2D plane stress (Bobaru and Zhang 2015). E is Young's modulus of

the material, δ is the horizon size, and h is a history-dependent scalar-valued function given as

$$h(\boldsymbol{\xi}, \boldsymbol{\eta}, T) = \begin{cases} 1 & \text{if } \quad s(\boldsymbol{\xi}, \boldsymbol{\eta}) - \alpha_T T < s_0, \\ 0 & \text{otherwise,} \end{cases} \quad (9)$$

where s_0 is the critical stretch determined by:

$$s_0 = \sqrt{\frac{5\pi G_0}{9k\delta}}, \quad (10)$$

for a conical micromodulus function in 2D plane stress (Bobaru and Zhang 2015). G_0 is the fracture energy (energy per unit fractured area for complete separation of the body in two halves), and k is the bulk modulus.

This material model is equivalent to the kernel function using $n = 1$ for peridynamic kernel $c(\hat{\boldsymbol{x}}, \boldsymbol{x}) / |\hat{\boldsymbol{x}} - \boldsymbol{x}|^n$ (see Chen et al. 2016). They constructed a peridynamic kernel ($n = 2$) based on physical principles for dynamic elasticity (and thermal diffusion) and showed that this is the only one whose convergence to the classical solution does not depend on the fineness of the discretization grid. Both models (with $n = 1$, or $n = 2$) converge, in the limit of horizon going to zero and ratio of horizon to grid spacing going to infinity, to the classical solution for problem with sufficient smoothness. Notice that for some kernel choices, the δ-convergence (when the horizon to grid spacing is kept constant as the horizon goes to zero) may lead to converged values that are different from the classical ones (Tian and Du 2013).

Here, we noticed no significant differences on crack patterns between $n = 1$ and $n = 2$, and the rest of the results in this paper use the kernel from the original PMB model ($n = 1$). The local damage at a point is defined as (Silling and Askari 2005)

$$D(\boldsymbol{x}) = 1 - \frac{\int_{\mathcal{H}_x} h(\boldsymbol{x}, \boldsymbol{\xi}, \boldsymbol{\eta}, T) \mathrm{d}V_\xi}{\int_{\mathcal{H}_x} \mathrm{d}V_\xi}. \quad (11)$$

According to Eq. 2, the force density on node i is discretized as

$$\boldsymbol{F}_i = \sum_{j \in \mathcal{H}_i} \boldsymbol{f}\left(\boldsymbol{x}_j - \boldsymbol{x}_i, \boldsymbol{u}_j - \boldsymbol{u}_i, \frac{T_j + T_i}{2}\right)$$
$$\Delta V_j + \boldsymbol{b}_i = 0, \quad (12)$$

where i and j are node numbers, ΔV_j is the reference volume of node j. Notice that the HHB partial volume correction (Bobaru and Zhang 2016) is applied to improve the accuracy of mid-point quadrature scheme because node j may not be fully covered within the horizon of node i.

Solving the nonlinear system in $\boldsymbol{u}_i$ of Eq. 12 is equivalent to minimization of the potential energy with respect to the nodal coordinates of all discretization nodes. The negative gradient of the total potential energy with respect to the current nodal coordinates of node i is $\boldsymbol{F}_i$. Starting from a starting guess for $\boldsymbol{u}_i$ given by unrestricted thermal expansion of the plate, we use the nonlinear conjugate gradient (NCG) method, like in (Zhang et al. 2016), to find the solution for the system in Eq. 12 for the starting given temperature profile. After each "translation" of the experimentally-measured or analytical temperature field (see Sect. 3 for details), the starting guess for NCG is the displacement field obtained by the NCG solver on the previous temperature field.

The NCG method is modified from sections B4 and B5 in Shewchuk (1994), and is shown in Algorithm 1. Here we use the secant method for the line search and the Polak–Ribière formula for calculating the value of β. The line search convergence criterion is defined as:

$$\alpha^2 \delta_d > \varepsilon_{\mathrm{LS}}^2 s_0^2 \Delta x^2, \quad (13a)$$

where α is a coefficient (see Algorithm 1), δ_d is the dot-product of search direction $\boldsymbol{d}$ with itself, Δx is the grid spacing, and $\varepsilon_{\mathrm{LS}}$ is the error tolerance for line search, equal to 10^{-5} in this study. The NCG convergence criterion is defined as:

$$\sum_i \boldsymbol{F}_i^2 < N_{\mathrm{DOF}} \cdot \varepsilon_{\mathrm{CG}}^2 \cdot F_{\mathrm{bmax}}^2, \quad (13b)$$

where N_{DOF} is the number of degree of the freedom in the system, $\varepsilon_{\mathrm{CG}}$ is NCG error tolerance, taken here as 5×10^{-5}, and F_{bmax} is the maximum allowable bond force (when $s = s_0$) given as

$$F_{\mathrm{bmax}} = cs_0 \Delta V, \quad (14)$$

where ΔV is the volume of a node assuming uniform grid. Error tolerance $\varepsilon_{\mathrm{LS}}$ and $\varepsilon_{\mathrm{CG}}$ were chosen sufficiently small that ensures no noticeable crack path differences when smaller convergence tolerances values are used.

Algorithm 1 Nonlinear conjugate gradient solver

```
1:    i_CG = 0
2:    i_LS = 0
3:    i_reset = 0
4:    r = F(u)
5:    d = r
6:    s = r
7:    σ_0 = 1/(cΔx)
8:    δ_new = r^T r
9:    While i_CG < i_CG,max and δ_new > N_DOF · ε_CG^2 · F_bmax^2
10:       i_LS = 0
11:       δ_d = d^T d
12:       α = −σ_0
13:       u_t = u + σ_0 d
14:       η_prev = [F(u + σ_0 d)]^T d
15:       Do
16:           η = [F(u)]^T d
17:           α = α η/(η_prev − η)
18:           u = u + αd
19:           η_prev = η
20:           i_LS = i_LS + 1
21:       While i_LS < i_LS,max and α^2 δ_d > ε_LS^2 s_0^2 Δx^2
22:       r = F(u)
23:       δ_old = δ_new
24:       δ_new = r^T r
25:       δ_mid = r^T s
26:       s = r
27:       β = (δ_new − δ_mid)/δ_old
28:       i_reset = i_reset + 1
29:       If i_reset = n_reset or β ≤ 0
30:           d = r
31:           i_reset = 0
32:       Else
33:           d = r + βd
       i_CG = i_CG + 1
```

The static solver in algorithm 1, in conjunction with the bond-failure criterion (exclusively based on critical tensile strain in a bond, see Eqs. 9 and 10) has been successfully applied to predict mode-I-dominated brittle fracture under fatigue conditions (see, e.g., Zhang et al. 2016). The critical tensile strain criterion, however, has its performance affected when mode-II fracture is an important component of mixed-mode failure. As we shall see in Sect. 4.1, the oscillating behavior of thermally-driven cracks in glass is such a case of mixed-mode cracking (mode-I-dominated and with a sign-changing mode-II, see Sakaue et al. 2009). We will show that small amounts of temporary shear deformations, that otherwise create a full crack in the physical experiment, leave some "leftover", unbroken bonds that continue to bridge the partial crack, when the criti-

cal tensile strain criterion alone is applied in our peridynamic model (see Sect. 4.1 for details). These unbroken bonds further affect the search direction in the energy minimization Algorithm 1 and lead to false (unphysical) minima corresponding to a fast damping of the oscillating crack. To eliminate this problem, we introduce a new and simple extra failure criterion that does not require tracking of the crack path and ensures leftover unbroken bonds from these small, transient shears, break, when getting near, but not passing, their critical strain.

3 System setup

In the experiment, the glass plate thickness is usually smaller than the diffusion length at low plate speed (Ronsin et al. 1995). Therefore, the temperature profile through the thickness and width can be considered as constant. In addition, the effect of crack growth on the temperature profile can also be ignored. Therefore, the slow thermal cracking can be considered as quasistatic, as long as the temperature profile is updated to mimic the conditions in the experiment. Note that we could also solve the transient heat problem with peridynamics (see e.g. Bobaru and Duangpanya 2010, 2012) but given the experimental details of the thermal field provided in the experiments (Ronsin and Perrin 1998), this is not necessary here. We thus account for the effect of the plate velocity v only via a "moving" temperature profile $T(x)$ imposed along the plate's length, as a function of the coordinate x along the glass plate's length direction.

The problem is modeled using 2D plane stress assumptions and a sketch of the simulated system is shown in Fig. 1. The glass slide with a small precrack (45° tilted or 0° horizontal, 1 mm long) at edge is immersed into the cold water bath with a constant velocity v. The steady-state thermal field (corresponding to the plate velocities shown in Fig. 1 bottom panel) is applied, and translated between the quasistatic thermos-elastic solutions with a small advancement step (from left side of the plate to the right) relative to the discretization grid spacing (see Table 1). This stepping strategy ensures converged crack paths, and is equivalent to allowing a certain number of bonds to break between static iterations used in modeling fatigue crack growth with PD (Zhang et al. 2016). Far away from the hot end of the gap (> 5 mm into oven), the region is considered inactive in NCG solver in order to
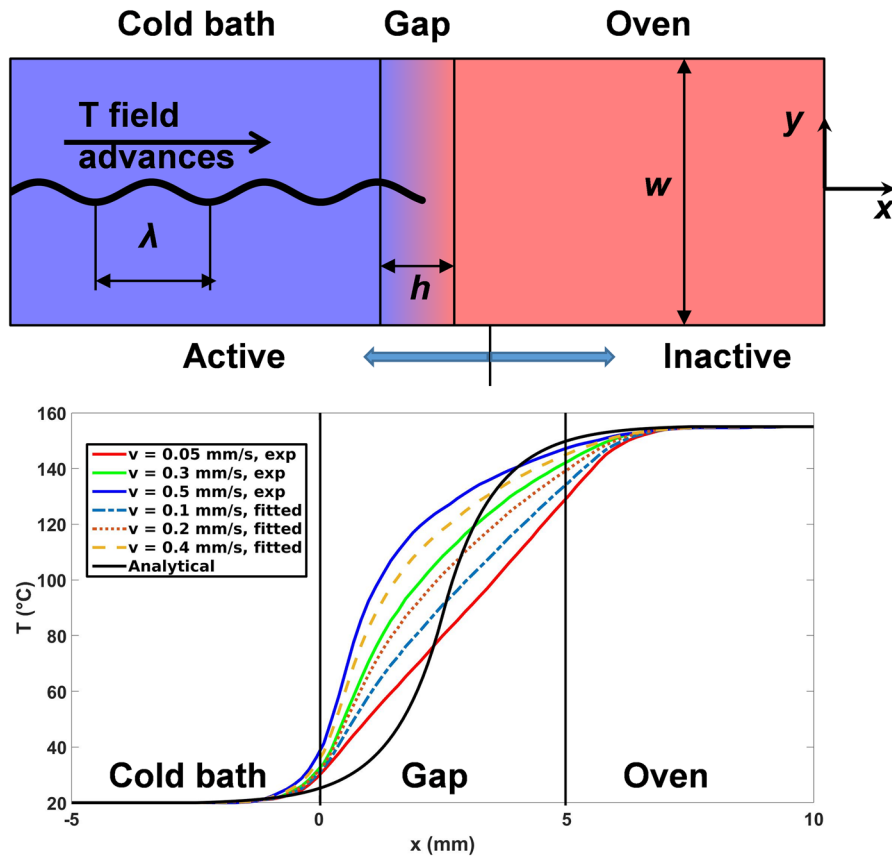
Fig. 1 Top: model setup with glass slide immersed into cold water bath with constant velocity v. A steady-state thermal gradient (relative to the cold front) leads to stable crack growth with propagation speed similar to the plate immersion speed. Region far from the hot end of the gap (> 5 mm) is considered inactive (fixed coordinates in NCG solver), to save computations. Bottom: Temperature fields input in the PD model. Steady-state thermal fields for three plate velocities ($v = 0.05, 0.3, 0.5$ mm/s) from experimental data in Ronsin and Perrin (1998). Notice temperature transition regions inside cold bath and oven. Thermal fields for plate velocities $v = 0.1, 0.2, 0.4$ mm/s are obtained by linear interpolation from nearest available experimental data. The analytical thermal field (applied in qualitative studies in Sects. 4.1, 4.2) is from the formula shown in Appendix A1 (see Eq. A1)

Table 1 Material properties for soda-lime glass, the sample geometry, and PD simulation parameters

Material properties	E (GPa)	ρ (kg/m^3)	G_0 at 30 °C (J/m^2)
	72	2440	3.8
Geometry	Width w (mm)	Gap h (mm)	Length L (mm)
	4–18	5	30
PD parameters	δ (mm)	m^a	Cold front increment (mm)
	0.4, 0.2	6	0.015

$\delta = 0.4\,mm$ is applied to the qualitative studies in Sects. 4.1 and 4.2, while $\delta = 0.2\,mm$ is used in the quantitative studies in Sects. 4.3–4.6
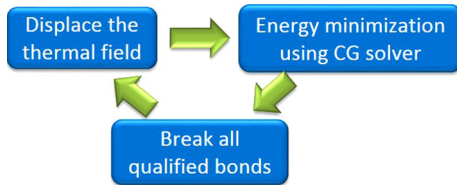[a] m is the relative grid density defined as the ratio of horizon size to the grid spacing

Fig. 2 The PD simulation cycle: advance the cold front over the sample by a small increment; solve the nonlinear system using NCG; break all qualified bonds based on the critical bond strain criteria (Eqs. 9 and 10) and correction criteria (Eq. 16); repeat

save computations in the PD simulation. Therefore, we only solve the system to the left of the active/inactive boundary in Fig. 1 top panel.

The corresponding steady-state thermal fields for three plate velocities ($v = 0.05, 0.3, 0.5$ mm/s) were digitized from experimental curve (see Fig. 2 in Ronsin and Perrin 1998) using about 100 data points (Fig. 1 bottom panel). Notice that the transitions of the temperature between three zones occur over a distance of a few mm (less than 10 mm) in experiments. The thermal field for three other plate velocities ($v = 0.1, 0.2, 0.4$ mm/s) were obtained using weighted average below:

$$T_v(x) = \frac{\left(T_{v1}(x) \times \ln\left(\frac{v_2}{v}\right) + T_{v2}(x) \times \ln\left(\frac{v}{v_1}\right)\right)}{\ln\left(\frac{v_2}{v_1}\right)},$$
(15)

given $v_1 < v < v_2$. $T_{v=0.1}(x)$ and $T_{v=0.2}(x)$ were calculated from the weighted average of $T_{v=0.05}(x)$ and $T_{v=0.3}(x)$, and $T_{v=0.4}(x)$ from the weighted average of $T_{v=0.3}(x)$ and $T_{v=0.5}(x)$. The temperature at any other location on the glass plate is obtained via a "local" cubic spline interpolation built using two nearest data points to the left, and two to the right of the specific location. An analytical thermal field was also used in the qualitative studies in Sects. 4.1 and 4.2. The expression for the analytical thermal field can be found in Appendix A1.

The measured fracture energy as a function of the temperature (Fig. 11 in Ronsin and Perrin 1998) is used to compute the temperature-dependent s_0 using a fitted curve (see Appendix A2). The velocity dependence of fracture energy within the plate velocity range 0.05–0.5 mm/s does not appear to be significant (see Fig. 10 in Ronsin and Perrin 1998) and thus is not considered in this study.

Figure 2 illustrates one PD simulation cycle in our model. The thermal field advances over a small spatial increment, then energy minimization is performed

using the NCG solver and all qualified PD bonds are broken based on the critical strain criterion. At this step, NCG solver should be run until no more bonds break, before moving the temperature field over the sample for the next iteration. However, because we use a sufficiently small advancement of the thermal field, we noticed no significant differences in the solutions when the "re-equilibration" part is skipped. The simulation cycle is repeated until the cold front advances a sufficiently long distance.

In order to make a direct quantitative comparison with Rosin's experimental work (Ronsin et al. 1995; Ronsin and Perrin 1998), soda-lime glass with same material properties is used in our simulation. Material properties and simulation parameters are listed in Table 1. A uniform 2D square grid is used to generate the nodal coordinates and the corresponding nodal areas.

A typical simulation consists of 1600 steps, which equals 24 mm on the advance of the cold front. The energy minimization with the NCG solver is performed on each step; it usually takes up to a few thousands cycles of the NCG algorithm to find the configuration corresponding to the energy minimum. The computational cost increases significantly when the horizon size decreases and with increasing value of m. m is the relative grid density defined as the ratio of horizon size to the grid spacing. GPU acceleration helps in this case, and the static solver in the PD simulation is accelerated by more than 100 times (single GPU vs CPU single core). This acceleration makes simulations of a system with one half-million nodes affordable (running in a few days). The implementation of the simulation on GPU is performed using CUDA and CUBLAS libraries (NVIDIA).

4 Numerical results

4.1 Leftover unbroken bonds across the crack and additional bond failure criterion

First, we qualitatively analyze the growth of thermally driven cracks on a setup similar to that in (Bouchbinder et al. 2003; Pham et al. 2008). The simulations are performed on a pre-notched (45° tilted, 1 mm long) soda-lime glass plate with material properties and geometry listed in Table 1. The glass plate has a width $w = 10$ mm, length $L = 30$ mm. The gap length $h = 5$ mm and an analytical thermal field (see
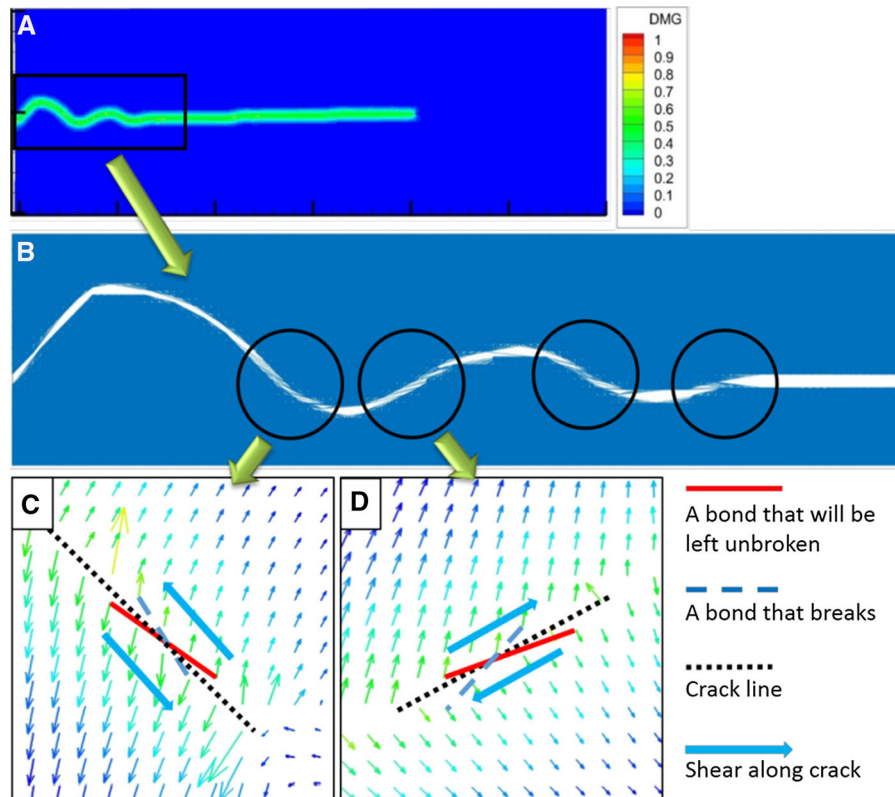
Fig. 3 Effect of leftover unbroken bonds across the crack and inspiration for the extra bond-failure criterion. **a** Attenuating crack path oscillations and high sensitivity to small changes in temperature gap or plate width. **b** A plot of the PD bond connectivity shows a large amount of leftover unbroken bonds across the crack (black circle), which affects the next static solution and leads to unphysical local minima. **c**, **d** Zoom-in on the "velocity" vector plots (displacement difference between two consecutive static solutions) at the crack tip area show that nodes on the opposing sides of the crack move away from each other but not perpendicular to the crack line (black dot line). This asymmetric movement on opposite sides of the crack line indicates existence of shear motion, which leads to some leftover unbroken bonds (red lines) bridging the crack. This shear motion changes direction as the crack advances towards the other side of the plate; this leads to the different orientations of the bridging bonds (see **c** and **d**). The "velocity" vector plots in **c** and **d** are taken when the crack tip is nearby, not for the final state shown in **b**

Fig. 1 bottom panel and Appendix A1) was applied due to its easier implementation (see black line in Fig. 1, bottom panel). Similar theoretical thermal fields were used in other studies (see e.g. (Bouchbinder et al. 2003; Pham et al. 2008). We use a relatively large horizon size $\delta = 0.4$ mm (1/25 of plate width w) and $m = \delta/\Delta x = 6$. The theoretical thermal field translates from left to right with a step size of 0.015 mm between iterations, which is 0.0375 relative to the horizon size.

Our first attempt to simulate thermally-driven crack growth in a glass plate showed signs of oscillating cracks. However, the oscillating cracks attenuate rapidly (die-off) and the crack continues to grow as a straight crack (see Fig. 3a), independent of temperature input conditions. In addition, we noticed only a very

small range of temperature, compared to what is seen in experiments, over which we obtain the oscillation behavior. Outside of this range (of a few degrees centigrade), we either get straight crack growth or branching cracks. The same sensitivity is noticed in terms of plate width changes.

To understand the reasons behind this behavior, we plot the bonds connectivity in Fig. 3b. We observe that there are many leftover, unbroken bonds bridging the crack (see circles in Fig. 3b). Such bonds form a small angle with the local crack direction, and suffer relatively small thermomechanical deformations, including small shear (see Fig. 3c, d), only for the period when the thermal gradient is present at that particular location. These small shear, temporary deforma-
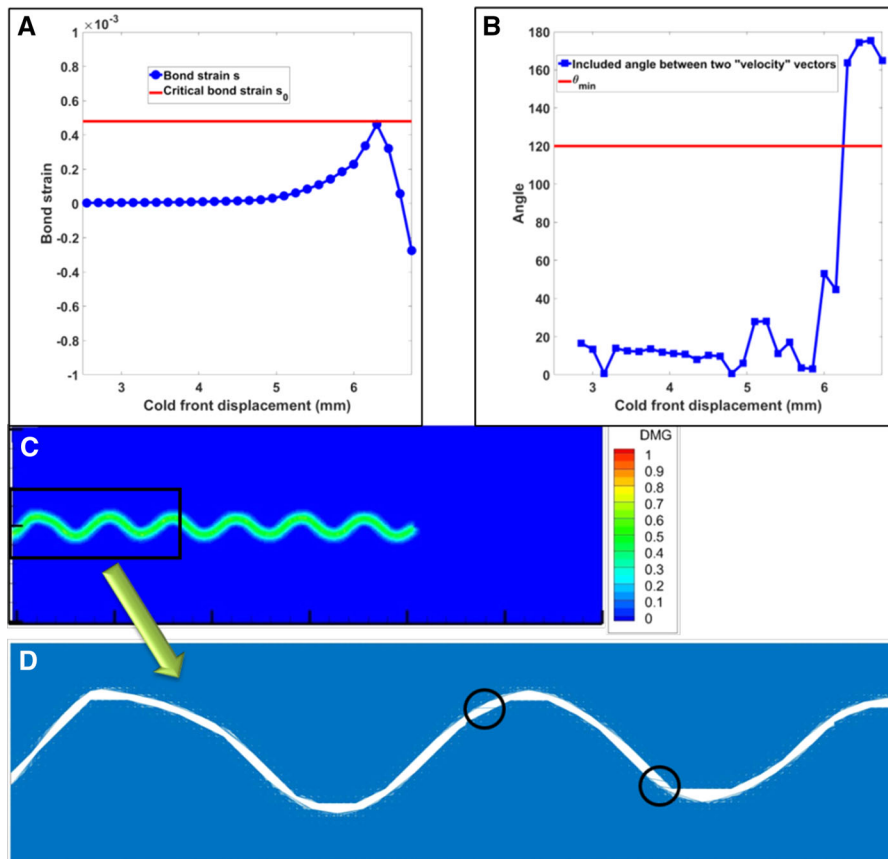
Fig. 4 The extra bond-failure criterion. **a** Strain history in a bond that will be left unbroken (red line in Fig. 3c) by the regular criterion. The critical bond strain s_0 given in Eq. 10 is approached but never passed, as the crack tip advances by the bond location. **b** The angle between the velocity vectors of this bond's end-nodes shows that nodes are moving away from each other (angle $>$ 120°) when the bond strain approaches s_0. This generated one of two conditions in the extra failure criterion. The other condition comes from the observation of high damage index on nodes along the crack line. **c** Smooth and stable oscillating crack is obtained after extra failure criterion is applied (Eq. 16). **d** Only few unbroken bonds remain when the extra failure criterion is used. Several leftover bonds still exist (black circles) only because damage index at one of the nodes is slightly lower than the D_{min} used. The effect of these bonds on crack path is negligible

tions are not sufficient to induce failure in all bonds crossing the growing crack (Fig. 4a). The critical bond strain criterion is not satisfied for all bonds in the crack region when small and temporary amounts of shear are applied. This is a deficiency of the current bond failure criterion, which is limited to bond-breaking in tension only.

The computations show that the shear motion changes sign as the crack tip advances in an oscillatory manner, which agrees well with the experimental observations that mode-II stress intensity factor K_{II} changes sign in accordance with the variation of the y-coordinate of the crack tip location (Sakaue et al. 2009; Yoneyama and Sakaue 2014). The sign change of the shear component leads to the orientation switch (seen in Fig. 3c, d) for the leftover unbroken bonds at different phases of the oscillation. Note that a peridynamic form of the J-integral for mode I loading has been introduced in (Hu et al. 2012), where it was shown that, in the limit of the horizon going to zero, the peridynamic J-integral converges to the classical value of the J-integral.

Once the temperature profile moves over, the local thermal strain gradients subside fast, and these bonds will never break. These unbroken bonds, however, further affect the search direction in the energy minimization algorithm and lead to false (unphysical) minima corresponding to the observed fast damping of the oscillating crack.

To remove the unbroken bonds across the crack, a general bond-breaking criterion that accounts for shear failure should be introduced. For the time being, we propose an extra bond-failure criterion added to the existing critical bond strain failure criterion (Eqs. 9 and 10) that causes bond breaking via tensile strain in the bond.

An investigation of the nodes' motion near the crack tip illustrates that nodes on two sides of the crack surface move away from each other (Fig. 3c, d), with the angles between their corresponding "velocity" vectors being very large (Fig. 4b). For a quasi-static problem, we define the nodal "velocity" vectors as the displacement vector between two consecutive static solutions.

Based on these observations, the extra bond failure criterion we introduce is: break the bond connecting node i and node j if

$$\text{both} \quad D_i \quad \text{and} \quad D_j > D_{\min}, \tag{16a}$$

and

$$\frac{v_i \cdot v_j}{|v_i| \, |v_j|} < \cos(\theta_{\min}), \tag{16b}$$

are satisfied. Here, D_i is the damage index on node i, v_i is the velocity of node i which equals the node displacement difference from previous step, $D_{\min}$ and $\theta_{\min}$ are parameters chosen to be $0.3°$ and $120°$ in this work. The first condition in the extra criterion ensures that nodes i and j reside on or near a crack surface, while the second condition guarantees that nodes i and j are located on opposite sides of the crack. A close look into the bond connectivity in Fig. 3b shows that the unbroken bonds exist for nodes within a layer smaller than the horizon size, away from the crack surface. The damage index at such nodes is larger than about 0.3. For a straight crack, nodes on opposite sides of the crack surface near the crack tip move away from each other in almost 180° (see Fig. 4b). However, for a curved crack, this angle can be lower than 180° . We choose $\theta_{\min} = 120°$ to allow such tolerance but still disqualify bonds connecting nodes that are on the same side of the crack surface.

We emphasize that the introduction of this extra condition only perturbs the system infinitesimally, because the bonds to which is applied, are very close to being broken at the moment when the conditions in Eq. 16 apply (see Fig. 4a, b). Moreover, although the extra bond failure criterion is applied over the entire simulation domain, it only becomes active at pairs of nodes

that reside on different sides of the crack and which are moving away from each other with a very large angle between their corresponding "velocity" vectors. The criterion does not influence the advancement of the crack tip because damage indices for nodes slightly ahead of the crack tip region do not satisfy the condition given in Eq. 16a.

The results in Fig. 4c show an extremely stable, periodically oscillating crack obtained after the implementation of the extra bond-failure criterion. The bond connectivity plot also verifies that almost all the leftover unbroken bonds (Fig. 4d) are eliminated and a very "clean" crack surface is obtained. A few leftover unbroken bonds still exist (black circles) because the damage index at one of the end-nodes was slightly lower (0.29) than the value we ran the test with, $D_{\min} = 0.3$. The effect of these few bonds on the crack path are, in any case, negligible. A safer value for this parameter would be $D_{\min} = 0.25$.

4.2 Transition of crack propagation regime with increase in temperature gap

We first investigate the transition of the crack propagation type with the increase in temperature gap, using the theoretical (analytical) thermal field, same material properties, and same glass plate geometry as in Sect. 4.1. Figure 5 clearly shows the transition of the crack shape from straight ($T_{gap} = 141 °C$, Fig. 5a), to dying oscillating ($T_{gap} = 163 °C$, Fig. 5b), to stable oscillating ($T_{gap} = 181 °C$, Fig. 5c), to branching ($T_{gap} = 221 °C$, Fig. 5d), to oscillating-branching hybrid ($T_{gap} = 281 °C$, Fig. 5e), to multiple branching ($T_{gap} = 381 °C$, Fig. 5f), under higher and higher temperature gap. The straight crack, stable oscillating cracking, and oscillating-branching hybrid crack are in excellent agreement with the experimental observations (see Fig. 5h–j) in Yuse and Sano (1993), obtained for similar type of conditions in thin Borosilicate glass plate). The dying oscillating crack matches extremely well with experimental observations (see Fig. 11 in Sakaue et al. 2009). Figure 5g illustrates the crack growth using a horizontal pre-crack (placed slightly off-center to introduce a small initial asymmetry), which reproduces the stable oscillating crack obtained using a 45° tilted pre-crack (Fig. 5c). We conclude that the oscillating crack with constant wavelength are highly stable in our computations, and are not sensitive
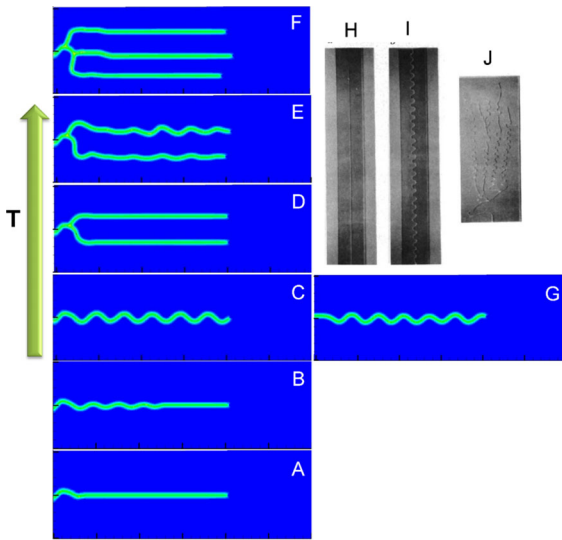
Fig. 5 Transition of the crack path from straight (**a**), to dying oscillations (**b**), to stable oscillations (**c**), to branching (**d**), to oscillating-branching hybrid (**e**), to multiple branching (**f**) with an increase in temperature gap. Crack patterns in **a**, **c**, **e** match experimental results in **h**, **i**, and **j**, in (Yuse and Sano 1993), respectively. The crack pattern in **g** is obtained under the same conditions as that in **c**, except for the horizontal pre-crack (placed slightly off-center to introduce a small asymmetry), instead of the 45° tilted pre-crack used in **c**. The development of stable oscillating crack initiates from different types of asymmetries and is not sensitive to the direction of the pre-crack
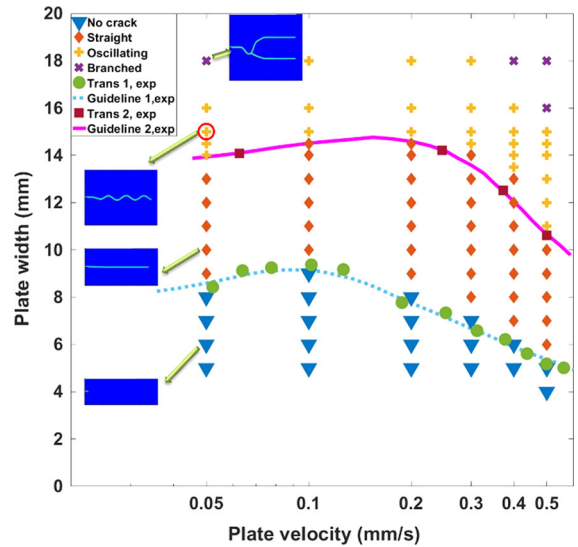

Fig. 6 Morphology phase diagram of crack transition in terms of plate velocity v against plate width w. Different crack patterns computed by the model are marked by (▼) for no crack growth, (♦) straight crack, (✚) oscillating crack, and (✖) branched crack. Inset images show actual crack paths computed for $v = 0.05$ mm/s at different plate widths w. Experimental delimiters $w_c(v)$ (■) and $w_{osc}(v)$ (●) from Ronsin and Perrin (1998) are shown with their corresponding guidelines (pink straight line and cyan dash line). Our model captures the nonlinear shape of the transition curves in this regime. The configuration marked by the red circle is used in the δ-convergence study

to the type of pre-crack from which they are generated. Note that experiments do mention the high reproducibility of this type of crack growth in glass plates (Yuse and Sano 1993).

It has to be pointed out that although we are capable of producing branching cracks with the static solver when the temperature gap is high, a dynamic solver for the coupled thermo-mechanical problem would be more appropriate in this regime. In experiments (Yuse and Sano 1997; Yang and Ravi-Chandar 2001), branching is induced at the higher immersion speeds (and/or higher temperature gap, and/or larger plate width). The approximation of the temperature field as steady-state is likely departing from the real situation. This is the reason for which this regime should be modeled by using a coupled transient thermomechanical PD model, in 3D (because the transient heat transfer through the thickness of the plate would also play a role in this case).

4.3 Phase diagram for crack types

Convergence studies (δ-convergence) for PD quasi-static models using the same solvers as in this work

have been reported in (Zhang et al. 2016) for modeling fatigue crack growth. Those simulations were performed with $m = 4$. A larger $m = 6$ is used in our study because a larger m produces less grid dependency of crack path (see Dipasquale et al. 2014). Larger m-values is always better from the point of view of accuracy, but is comes at a cost: the computational time scales with $O(m^2)$.

We conduct a δ-convergence study for thermally-driven fracture using $\delta = 0.4, 0.3, 0.2, 0.15$, and 0.1 mm with $m = 6$, respectively. The physical parameters are as follows: plate immersion speed $v = 0.05$ mm/s, plate width $w = 15$ mm, temperature gap $T_{gap} = 135\,°C$ (see location marked by the red circle in Fig. 6). *These conditions are especially delicate because they are near the separation, in the phase diagram, between oscillating crack and straight crack growth behavior observed in experiments.* The experimental thermal field (see Fig. 1 bottom panel) is applied. This plate width $w = 15$ mm, turns out to be only 1 mm above the critical plate width w_{osc} (which

separates the straight crack growth behavior from the oscillating crack at this immersion speed, see column for $v = 0.05$ mm/s in Fig. 6).

Branching cracks are observed at $\delta = 0.4$ and 0.3 mm, while oscillating crack is observed when using $\delta = 0.2$ mm and lower (see Appendix A3). The crack path depends on the horizon size, up to a certain level, for two reasons:

(a) The "thickness of damage" changes with the horizon size (see Ha and Bobaru 2010). The amount and distribution of material on both sides of the crack is critical in this problem, since this distribution is what determines the amount of thermal strains, which in turn controls the crack path evolution (see Sect. 4.6). The smaller the horizon size, the less damaged material volume (with broken bonds) we get; an imbalance between the amount of material to the left and right of the advancing crack line is smaller when the same small quantity is "shaved off" both side than when the same, but larger amount is removed from both sides; as a result, decreasing the horizon size leads to a reduction in the amplitude of oscillations of an undulating crack path, or, a higher entropy behavior switches to a lower one (e.g. branching transitions to oscillating crack, oscillating cracks transitions to straight crack, straight crack to no crack), if we are near a transition demarcation zone in the phase diagram.

(b) The sharpness of the temperature gradient recovered by the PD solution depends, up to a point, on the horizon size (see Bobaru and Duangpanya 2010, 2012). When the horizon is large relative to the width over which temperatures changes rapidly which could be considered as a relevant length-scale in this problem (see Bobaru and Duangpanya 2012), the PD solution cannot approximate well the actual thermal strains and the computed contraction forces exerted around the crack tip, which influence the crack path (see Sect. 4.6), will differ from the real case. Once the horizon size is sufficiently small (relative to the length scale introduced by the temperature gradient) the thermal field matches the physical one.

The search for an "optimal" horizon size can be executed via the convergence study detailed in Appendix A3, which is really a "calibration" for the horizon size using data points near one of the separation boundaries between zones in the experimental phase diagram. Such a calibration procedure performed using a single point in the phase diagram is valid as long as using the "calibrated" horizon size recovers the entire experimental phase diagram. The convergence study in Appendix A3 gives a horizon of $\delta = 0.2$ mm as an "optimal" size for our test, and we shall see that such a horizon size is indeed able to recover the entire experimental phase diagram.

For the rest of the computations reported here we select and use $\delta = 0.2$ mm. With this horizon size, the ratio to the smallest geometrical dimension of all the plates considered here is $w/\delta = 20$ (see also Bobaru and Duangpanya 2012).

We perform a quantitative study for the crack type that results from the thermal loading discussed below, and compare results against the experimental ones from Ronsin et al. (1995), Ronsin and Perrin (1998). For a fair comparison, we use the same soda-lime glass as that listed in these experiments. Thermal field profiles at different plate velocities were extracted from experimental measurements in Ronsin and Perrin (1998), or interpolated from the nearest available experimental data in that paper, if not provided in there. A temperature-dependent fracture energy is fitted from the experimental measurements (see Fig. 12 in Appendix A2).

Simulations of crack growth with six different immersion velocities ranging from 0.05 to 0.5 mm/s, and plate widths ranging from 4 to 18 mm were performed. The temperature difference T_{gap} between the oven and cold bath is kept as 135 °C. In our *quasistatic* simulations, plate velocity is not a direct input parameter. Instead, thermal field profiles corresponding to different plate velocities are provided. The thermal profiles effectively embed the "dynamics" in this problem: the immersion speed.

Figure 6 shows the phase diagram, computed with PD, for crack propagation type/mode, in terms of immersion velocity and plate width: no crack growth (▼), straight crack (♦), undulating crack (✚), and branching crack (✖). The lines in this plot are curve-fits to the experimental data (also shown) from Ronsin and Perrin (1998).

We ran tests for a grid of six immersion velocities by 14 plate widths, for $84 + 1 = 85$ (one extra for $w = 4$ mm) different configurations. In general, we observe that for lower immersion velocities and small plate widths, no crack grows from the pre-notch. When,

for a given immersion speed, w exceeds a certain critical value w_c, a crack starts to grow in a straight line. Crack path instability occurs when the plate width continues to increase above w_{osc}, where oscillating cracks are observed. When w is slightly beyond the onset of oscillations, the crack shape is almost sinusoidal. As w continues to increase, the amplitude of the, until now, uniform oscillations increases and the periodicity is no longer stable, eventually leading to branched cracks. Similar to the crack pattern transition observed in Fig. 5, the inset images in Fig. 6 show the transition from no crack ($w = 6$ mm), to straight crack ($w = 10$ mm), to oscillating crack ($w = 15$ mm), to branching ($w = 18$ mm) with the increase of plate width w, at the particular plate immersion speed $v = 0.05$ mm/s and for the temperature gap $T_{gap} = 135\,°C$. Movies showing the transient temperature field and growth of straight crack, oscillating crack, and branching crack can be found in the Supplementary material for two different immersion speeds (0.05 mm/s and 0.5 mm/s) and several plate widths (see Movies 1–5).

It is interesting to note that, for a certain plate width, the computed PD results show that surprising situations of the following kind are possible for a plate of fixed width: oscillating crack happens at a lower immersion speed, straight crack growth at intermediate speed, and a return to oscillating crack at higher speed. This "nonlinear" behavior is peculiar, but is it seen in reality? Surprisingly, yes! The extracted separation lines between these regions of crack-types from the experimental phase diagram given in (Ronsin and Perrin 1998) are shown on the same graph. The critical values w_c for the no-crack to straight-crack transition, and w_{osc} for straight-crack to oscillating-crack transition, are functions of plate velocity v. Ronsin and Perrin (1998) provide experimental values $w_c(v)$ (●) and $w_{osc}(v)$ (■) for some plate velocities, and we placed these values on the computed phase diagram in Fig. 6. We also use the guidelines (pink continuous and cyan dotted lines in Fig. 6) digitized from Ronsin and Perrin (1998) in our phase diagram for a direct comparison. Note that Ronsin and Perrin (1998) do not investigate the transition to branching regime.

The PD-computed and experimental separations between the different crack behavior regions in the phase diagram of Fig. 6 are almost identical. The perfect match includes the unusual nonlinear behavior mentioned above, in which a plate of a certain width may transition from no-crack to straight-crack, and
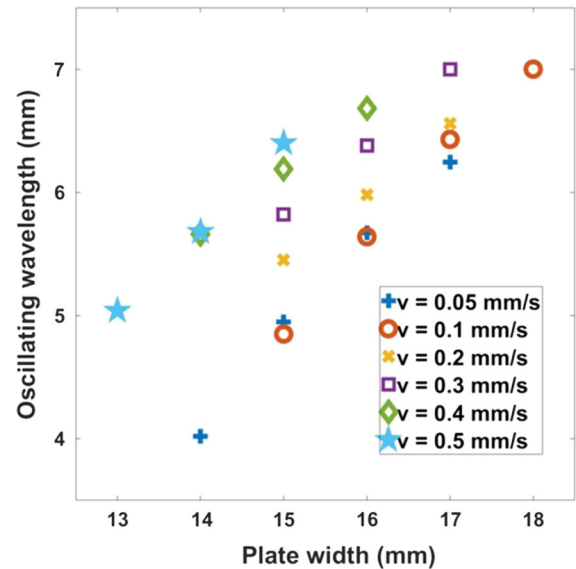

Fig. 7 Wavelength of the oscillating crack as a function of the plate width. A linear dependence is noticed for several immersion speeds

back to no-crack (or from straight-crack to oscillating crack, and back to straight-crack), with increasing immersion velocity. The maximum deviation in the separation lines in terms of critical plate width is within 1 mm across all plate velocities. It must be pointed out that only four experimental data points (■) were available for "straight" to "oscillating" crack transition within the velocity range studied here. Because of this, the guideline we drew for L_{osc} (pink line in Fig. 6) may not represent the actual separation line with high accuracy. The PD model captures the nonlinearity in both transition curves, noted in the experimental data (Ronsin and Perrin 1998).

We emphasize that our simulations only used the linear thermomechanical model, with damage modeled via the failure of PD bonds in tension based on the critical bond strain criterion (Eqs. 9 and 10) and the correction criterion (Eq. 16) for cracks growing under small and temporary shear deformations. The constant bond failure strain is equivalent to Griffith's criterion (Silling and Lehoucq 2010). No other explicit failure criteria based on energy, stress, or strain were used.

4.4 Oscillating wavelength

Figure 7 shows the wavelength of the oscillating crack as a function of the plate width for different

Fig. 8 Equilibrium crack tip location z_{tip} as a function of plate width w. Plate immersion speed $v = 0.1$ mm/s, gap distance between the oven and cold bath $h = 5$ mm, temperature difference $T_{gap} = 135\,°C$. Crack tip moves towards the hot oven entrance as the plate width increases (⧫). The available experimental results are for a plate immersion speed of $v = 0.125$ mm/s (●) (from Fig. 7 of Ronsin and Perrin 1998)
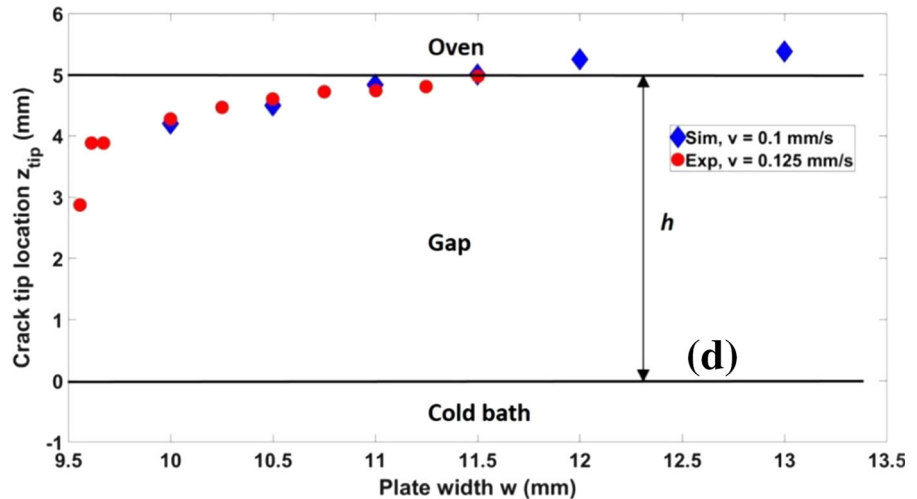

plate immersion speeds, with temperature gap fixed at 135 °C. Above the critical w_{osc}, the oscillating wavelength is approximately a linear function of the plate width. The wavelengths mostly fall in the range of 5–7 mm, which also match well the values reported in experiments (Ronsin and Perrin 1998). Specifically, the wavelength λ for $v = 0.2$ mm/s and $w = 15$ mm is about 5.7 mm, while the experimental value is 5.6 mm (see Fig. 13 in Ronsin and Perrin 1998).

4.5 Crack tip location

We computed the values for the equilibrium (after the crack has advanced a short distance into the plate) crack tip location z_{tip} at different plate widths w for a fixed plate velocity $v = 0.1$ mm/s, given gap distance between the oven and cold bath $h = 5$ mm, and given temperature difference $T_{gap} = 135\,°C$. Under these conditions, for plate widths in the range of 10–13 mm, the propagating crack path remains straight. As the plate width increases, more elastic energy is available and the crack tip stabilizes closer to the entrance in the hot oven, and may even enter slightly into the oven region for the larger plate widths (Fig. 8). This trend matches very well the experimental results performed under the same conditions, except with a slightly higher plate velocity $v = 0.125$ mm/s (see Fig. 7 of Ronsin and Perrin 1998).

4.6 Elastic vortices and instability of crack growth

To better understand the reasons behind the observed crack path instabilities, we find that probing the rel-

ative motion field (the "velocity" field, see Sect. 4.1) is very informative and rather fascinating. Collective elastic rotational motion of material points in an elastic solid (aka elastic vortex) was mentioned in Shilko and Psakhie (2014) in a study of dynamic mode II cracking, where the vortex velocity approached the shear wave speed. Elastic vortices were also observed in dynamic mode I cracking and branching in Bobaru and Zhang (2015) [see page 90 and Fig. 28 in Bobaru and Zhang (2015)]. Here we show that the elastic vortex is also relevant in quasi-static crack growth in quenched glass, where the vortex velocity (the translational speed of coherent structures, not the nodal velocities) is very small, below mm/s.

In order to visualize the streamlines of the nodal velocity field (see Sect. 4.1), the Linear Integral Convolution algorithm (Cabral and Leedom 1993; van Wijk 2002) was applied. First, the image pixels colored by the velocity vector magnitude is blended with a random black/white noise image. Then, the local behavior of the vector field at a pixel (x,y) is approximated by computing a local streamline that starts at this pixel and moves out in the positive and negative directions for a certain distance (e.g. 20 steps with step size of one pixel). The color at pixel (x, y) is calculated as the convolution of a suitable integral kernel with the color of all pixels in this streamline. Intuitively, this is similar to pouring color into a river.

Figure 9 illustrates the formation of elastic vortices ahead of the crack tip for different crack paths caused by different plate widths, while the temperature difference T_{gap} and plate immersion speed v are fixed at 135 °C and 0.2 mm/s, respectively. Even for a plate
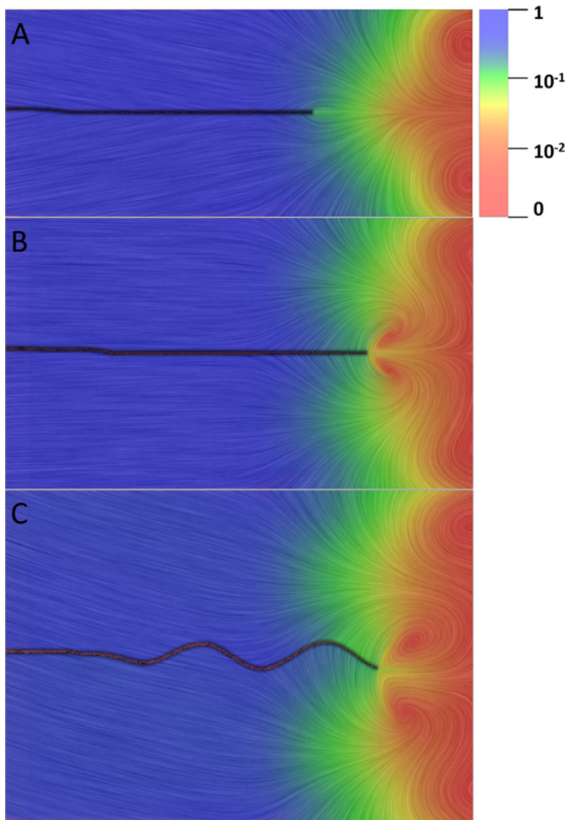
Fig. 9 Elastic vortices appear in the streamlines of the "velocity" field. Crack paths for different plate widths w, for the temperature gap $T_{gap} = 135\,^{\circ}\text{C}$, and plate immersion speed $v = 0.2\,\text{mm/s}$. **a** $w = 10\,\text{mm}$; **b** $w = 13\,\text{mm}$; **c** $w = 16\,\text{mm}$. The color indicates the relative magnitude of the "velocity" vector (normalized to [0 1] with 1 representing the maximum value, at the scale of $10^{-4}\,\text{mm/s}$, estimated from maximum displacement vector divided by the time interval between two consecutive static solutions)

without a crack, given the geometry and the thermal gradient over the plate, one would obtain the circular vortices noticeable near the top and bottom right side of the plate (in the oven). These symmetric vortices, relative to the center line, are always present. For the plate width $w = 10\,\text{mm}$ (Fig. 9a), the straight crack advances along the symmetry line, as if it is "drawn", as in metal sheet drawing between rollers, in this case the circular vortices. For a larger plate width, $w = 13\,\text{mm}$ (Fig. 9b), the crack maintains straight-line growth, but two symmetric vortices appear in the crack tip vicinity. The material points ahead of the crack tip move towards the crack tip, while for lower plate width $w = 10\,\text{mm}$ (for the same immersion speed and temperature gap) they move away from the crack tip (see videos in the Sup-

plementary material for the motion). It is interesting to point out that the transition from straight to oscillating crack does not coincide with the change of "velocity" vector direction ahead of the crack tip. The straight-to-oscillating transition was experimentally verified (see Yang and Ravi-Chandar 2001) to not match the change of T-stress sign, and therefore, the T-stress criterion (Cotterell and Rice 1980) for crack path instability is not applicable in this case.

At an even larger plate width, $w = 16\,\text{mm}$, as the contraction forces grow on the two sides about the crack (because the amount of material contracting as it is immersed in the cold bath, is larger), any small imbalance between them leads to the formation of elastic vortices that are no longer symmetric about the central line (see Fig. 10). When one such vortex becomes sufficiently "stronger" than its "twin", the crack moves in a direction as if it is pulled by the stronger elastic vortex towards it. Eventually, the material (and its associated contraction force) on the side opposite to the direction in which the crack grows becomes sufficiently large that the contraction force (and the velocity vortex associated with it) becomes dominant and it starts to turn the crack around, pulling the crack back. This process repeats, resulting in a constantly undulating crack path. In terms of velocity vortices, the continued competition between the strength of the "cyclones" surrounding the crack tip, which vary with the plate width, the immersion speed, and the temperature gap, leads to the growth of oscillating crack paths. This phenomenon reminds us of the coherent turbulent structure commonly seen in fluids (see, e.g., Hussain 1986).

At even larger plate widths and/or higher immersion speed (e.g. $w = 16\,\text{mm}$ and $v = 0.5\,\text{mm/s}$), branched cracks are produced (Fig. 11a). Here we are particularly interested in how crack branching develops (circled in Fig. 11a). Interestingly, the crack does not split in two at its tip, instead, a secondary branch starts from a point along the main crack. This happens because the larger amount of stored elastic energy in the wider plate leads to sharper turns in oscillating crack path, nearly perpendicular to the immersion direction (Fig. 11b); the combination between opening of a nearly vertical crack and shrinkage (thermal contraction due to cooling) of the glass plate creates a vortex that continues to pull the crack away from the immersion direction; however, this crack growth is slowed down as it starts to move perpendicular to the immersion direction, and its growth is not sufficient to release the stored elastic
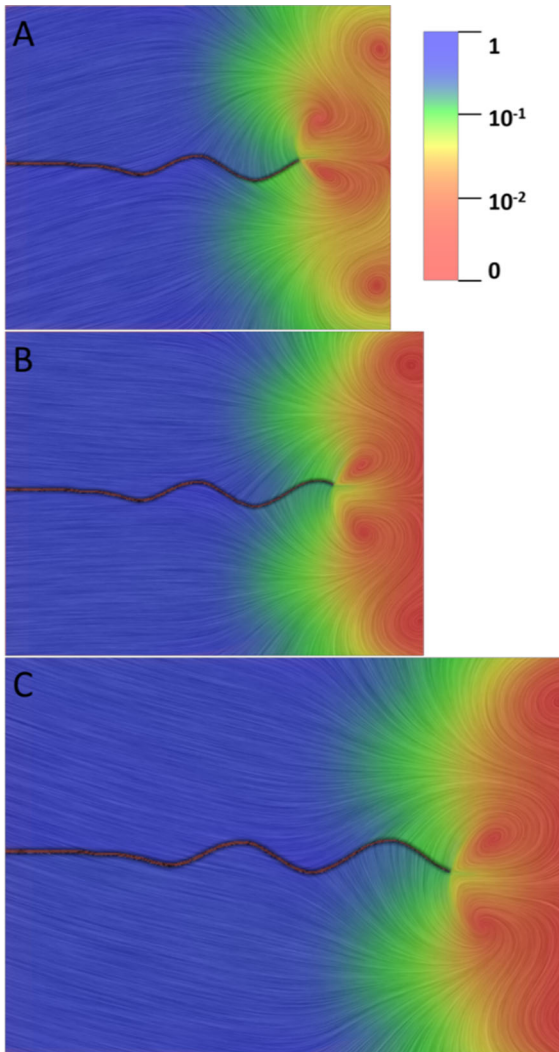
Fig. 10 Elastic vortices in the streamlines of the "velocity" field. Oscillating crack path at different phases for the temperature gap $T_{gap} = 135\,°C$, plate immersion speed $v = 0.2\,mm/s$, and $w = 13\,mm$: **a** before crack tip arrives at a max amplitude; **b** after the crack tip passes a max amplitude; **c** before crack tip reaches another maximal amplitude. Observe the competition between the coherent turbulent structures and the resulting path followed by the crack

energy caused by the thermal field. Therefore, a new crack branch develops around the turning point of the existing crack, where strain energy is now concentrated (Fig. 11c). The initiation of this secondary branch is happening under mode-I conditions.

While the new branch grows rapidly, the evolution of the thermoelastic deformations ahead of the crack tip of the original path "restart" its growth. The two branches now advance at almost the same pace (Fig. 11d). Notice
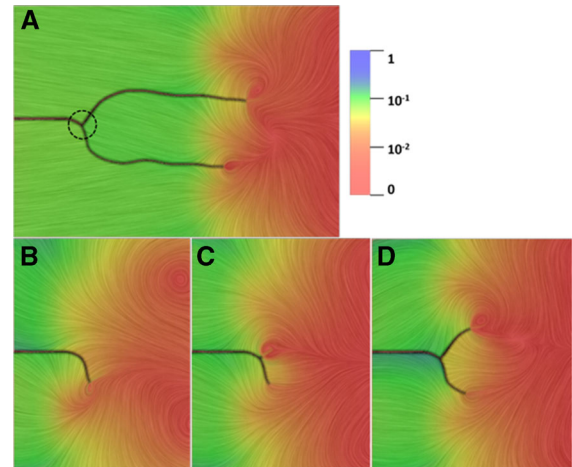

Fig. 11 Elastic vortices in the streamlines of the "velocity" field. **a** Full branched crack path for the temperature gap $T_{gap} = 135\,°C$, plate immersion speed $v = 0.5\,mm/s$, and $w = 16\,mm$. Snapshots show the development of a side branch (dashed circle in **a**): **b** before the side branch appears; **c** side branch tip emerges; **d** side branch continues to grow

that the two branches influence each-others growth (see the elastic vortices in Fig. 11a). Their spacing is relatively uniform (see also Fig. 5e, f), and when one oscillates (at higher immersion speed or larger plate widths), the other does it too, in tandem [see also Fig. 1 in Sakaue et al. (2008) for experimental results on this observation]. The streamlines for this case show many patterns similar to limit cycles and bifurcations seen in phase portraits for dynamical systems (see Strogatz 2001).

The "velocity" field for other plate widths in the case of immersion speed $v = 0.5\,mm/s$ can be found in Fig. 14 in Appendix A4. Movies of crack growth showing the velocity vortices for three different plate widths (10, 13, and 16 mm) and two different immersion velocities (0.2 mm/s and 0.5 mm/s) can be found in Supplementary material (see Movies 6–11).

5 Summary

We demonstrated computational predictability of slow-growth thermal cracking in glass for the specific set of experiments with a notched hot thin glass plate immersed into a cold bath. In contrast with previous attempts at simulating this type of experiments, we provide quantitative comparisons between our model's results and experiments. The new peridynamic model, with an improved fracture criterion that eliminates

"bridging bonds" left behind the crack front when very small and temporary thermo-mechanical shear deformations are present, reproduces in detail the crack-instability phase diagram obtained experimentally in Ronsin and Perrin (1998), as well as the crack tip location dependence on the plate width. The model captures the crack growth patterns (no crack growth, straight crack, oscillating crack, branching crack) that depend on the immersion speed and plate width, and matches perfectly the experimental observations of the transition curves between these regions. From the point view of motion of material points during the thermally-driven fracture process, we show that the growth of oscillating crack paths is a direct result of the competition between the relative strength of elastic vortices developed in the vicinity of the crack tip. For sufficiently large plate widths (for a fixed immersion speed and temperature gap), the contraction forces are strong enough to sustain elastic vortices that "pull" the crack back and forth leading to the propagation of an undulating crack path initiated by small asymmetry in the location of the pre-notch.

We discussed a method for determining the appropriate size of the peridynamic horizon based on data points at the separation between crack-type zones in the experimental phase diagram. For the immersion speeds tested in this paper ($v = 0.05-0.5$ mm/s range and temperature gap of 135 °C), a static peridynamic solver was sufficient to solve the problem (once the horizon size is smaller than the relevant length-scale in the problem induced by the thermal gradients, or the width over which the temperatures change fast). For cases in which the immersion speed or the temperature gap are significantly higher, a dynamic and fully coupled thermomechanical solver may need to be used.

The unrestricted growth of damage provided by the peridynamic model allowed autonomous crack growth in arbitrary directions, as well as initiation of secondary crack branches in thermally-driven crack growth. The simple peridynamic model used here shows that the complexities observed in quenched-glass fracture behavior can be predicted to the finest details. The interesting similarities between coherent structures observed in the velocity field of this problem and coherent structures in fluids or bifurcation diagrams of dynamical systems require further exploration.
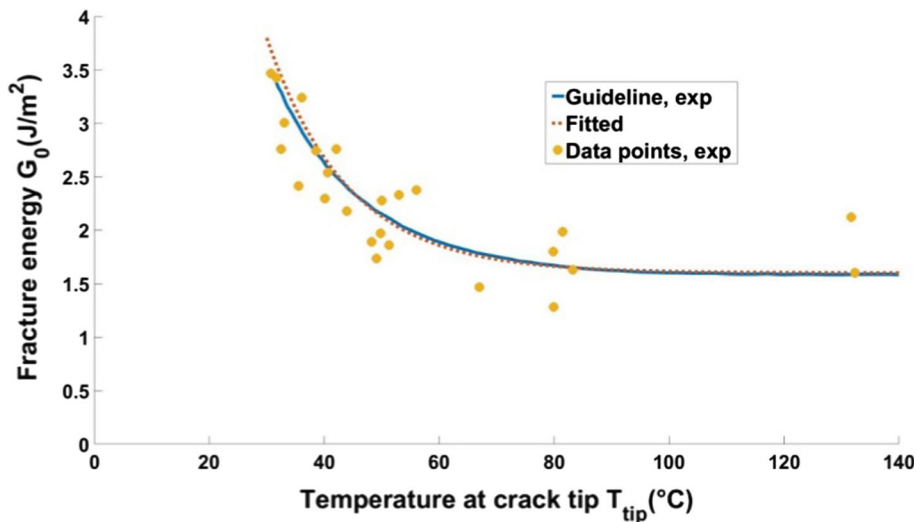
Fig. 12 Temperature-dependent fracture energy. The guideline (blue line) for the experimental data points (●) is fitted using Eq. A1 (red dot line). The experimental data are digitized from Ronsin and Perrin (1998)

Appendix A1: Mathematical expression of the analytical thermal field

An analytical expression, shown in Fig. 1, that approximates the thermal field from the water bath, across the gap, and into the oven, is (see Bouchbinder et al. 2003, Pham et al. 2008):

$$
T(x) = \begin{cases}
T_0 & if \ x \leq -H, \\
T_0 + \frac{1}{2} T_{\text{gap}} \left(1 - \frac{1 - exp\left(\frac{x}{L_D}\right)}{1 - exp\left(-\frac{H}{L_D}\right)} \right) & if \ -H < x \leq 0, \\
T_0 + \frac{1}{2} T_{\text{gap}} \left(1 - \frac{1 - exp\left(-\frac{x}{L_D}\right)}{1 - exp\left(-\frac{H}{L_D}\right)} \right) & if \ 0 < x \leq H, \\
T_0 + T_{\text{gap}} & if \ x > H,
\end{cases}
$$
$$(A1)$$

where $H = 10$ mm (double of the gap length h) to have a transition of the temperature between three zones similar to that observed in the experiment (see Fig. 1 bottom panel), T_0 the temperature of the cold water bath, T_{gap} the temperature difference between water bath and oven, $L_D = 1$ mm the diffusion length, and x the coordinate along length direction with the origin ($x = 0$) placed at the interface between the water bath and the gap.

Appendix A2: Temperature dependent fracture energy

Experiments showed that the fracture energy decreases with the increase of the temperature at the crack tip (● dots and corresponding blue guideline in Fig. 12, digitizied from Fig. 11 in Ronsin and Perrin 1998). To take this effect into consideration in our simulation, the guideline is fitted using the equation:

$$
\begin{aligned}
G_0 = G_{0,\text{min}} + \left(G_{0,\text{max}} - G_{0,\text{min}} \right) \\
\cdot \exp\left[-\beta \left(T - T_0 \right) \right],
\end{aligned}
$$
$$(A2)$$

where $G_{0,\text{max}} = 3.8$ J/m^2 and $G_{0,\text{min}} = 1.6$ J/m^2 correspond to the fracture energy at lower temperature limit temperature ($T_0 = 30\,°C$) and at higher temperature limit, respectively. $\beta = 1/14$ is a fitting parameter. Equation A2 represents the experimental G_0—T relation very well, for T above 45 °C. A slight deviation below 45 °C has no impact on the crack growth because the crack tip never falls in this low temperature region.
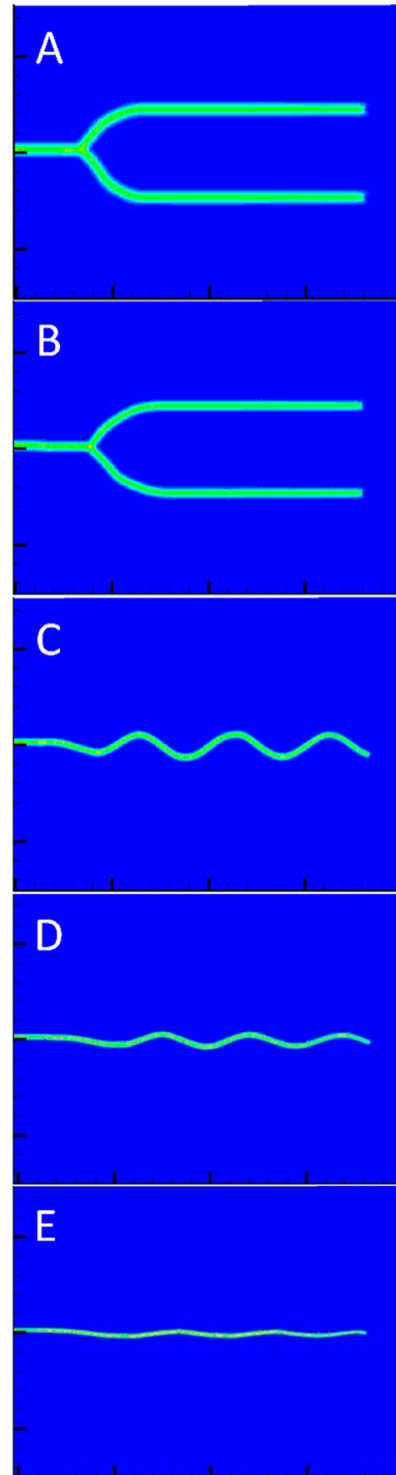

Fig. 13 Crack paths for different horizon sizes δ, while other parameters are fixed: **a** $\delta = 0.4$ mm; **b** $\delta = 0.3$ mm; **c** $\delta = 0.2$ mm; **d** $\delta = 0.15$ mm; **e** $\delta = 0.1$ mm. The m-ratio is 6
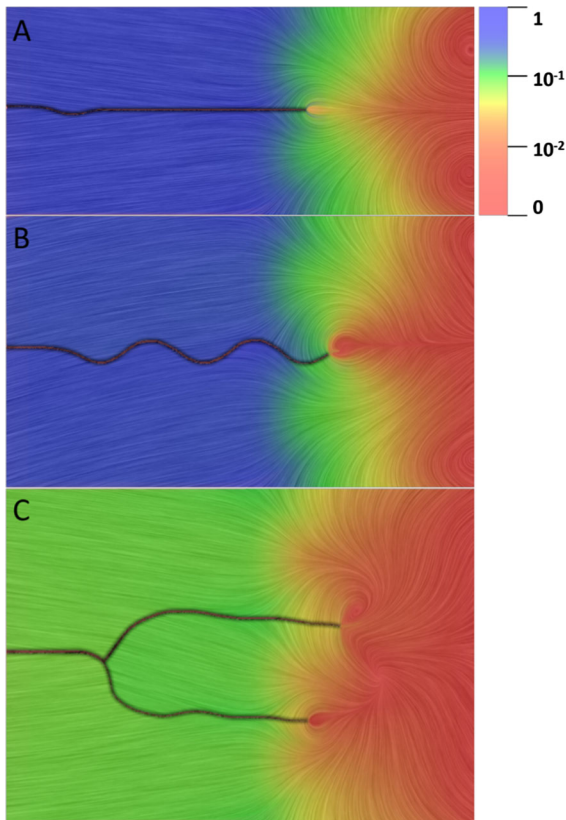
Fig. 14 Elastic vortices appear in the streamlines of the "velocity" field. Crack paths for different plate widths w, for the temperature gap $T_{\text{gap}} = 135\,°C$, and plate immersion speed $v = 0.5\,\text{mm/s}$. **a** $w = 10\,\text{mm}$; **b** $w = 13\,\text{mm}$; **c** $w = 16\,\text{mm}$

Appendix A3: δ-convergence

Figure 13 shows the crack path at different horizon size δ while other parameters are fixed: $T_{\text{gap}} = 135$ °C, immersing velocity $v = 0.05$ mm/s, plate width $w = 15$ mm, $m = \delta/\Delta x = 6$. On the physical phase diagram, the physical parameters place this case near the transition zone between growth of a straight crack and an oscillatory crack (see Fig. 6). Branching cracks are observed at $\delta = 0.4$ and 0.3 mm, while oscillating crack is observed at $\delta = 0.2$ mm and lower. The horizon size influences the amount of damage along the crack path. For a larger horizon, a larger amount of material is damaged and any small imbalance between the amounts of material on the sides of the crack path gets amplified more. As the horizon decreases, this imbalance approaches the physical, real imbalance, that leads to thermal strain larger on one side than the other, which

consequently results in contraction forces that pull the crack from its straight path into an oscillatory one. (see discussion in Sect. 4.3). Notice that for the oscillating crack case, the wavelength appears to be relatively insensitive to the horizon size, while the starting point of oscillations slightly moves farther from the notch tip the smaller the horizon is.

Appendix A4: Elastic vortex and instability of crack growth for $v = 0.5\,\text{mm/s}$

References

Bobaru F, Duangpanya M (2010) The peridynamic formulation for transient heat conduction. Int J Heat Mass Transf 53:4047–4059. https://doi.org/10.1016/j.ijheatmasstransfer.2010.05.024

Bobaru F, Duangpanya M (2012) A peridynamic formulation for transient heat conduction in bodies with evolving discontinuities. J Comput Phys 231:2764–2785. https://doi.org/10.1016/j.jcp.2011.12.017

Bobaru F, Hu W (2012) The meaning, selection, and use of the peridynamic horizon and its relation to crack branching in brittle materials. Int J Fract 176:215–222. https://doi.org/10.1007/s10704-012-9725-z

Bobaru F, Zhang G (2015) Why do cracks branch? A peridynamic investigation of dynamic brittle fracture. Int J Fract 196:59–98. https://doi.org/10.1007/s10704-015-0056-8

Bobaru F, Zhang G (2016) Crack branching in dynamic brittle fracture. In: Bobaru F, Foster JT, Geubelle PH, Silling SA (eds) Handbook of peridynamic modeling. CRC Press, Taylor and Francis Group, pp 245–316

Bouchbinder E, Hentschel HGE, Procaccia I (2003) Dynamical instabilities of quasistatic crack propagation under thermal stress. Phys Rev E Stat Nonlinear Soft Matter Phys 68:36601. https://doi.org/10.1103/PhysRevE.68.036601

Bourdin B (2007) Numerical implementation of the variational brittle fracture formulation. In: Combescure A, Belytschko T, de Borst R (eds) IUTAM symposium on discretization methods for evolving discontinuities. Springer, pp 381–394

Cabral B, Leedom LC (1993) Imaging vector fields using line integral convolution. In: Proceedings of the 20th annual conference on computer graphics and interactive techniques—SIGGRAPH '93. ACM Press, New York, NY, USA, pp 263–270

Chen Z, Bakenhus D, Bobaru F (2016) A constructive peridynamic kernel for elasticity. Comput Methods Appl Mech Eng 311:356–373. https://doi.org/10.1016/j.cma.2016.08.012

Corson F, Adda-Bedia M, Henry H, Katzav E (2009) Thermal fracture as a framework for quasi-static crack propagation. Int J Fract 158:1–14. https://doi.org/10.1007/s10704-009-9361-4

Cotterell B, Rice JR (1980) Slightly curved or kinked cracks. Int J Fract 16:155–169. https://doi.org/10.1007/BF00012619

Dipasquale D, Zaccariotto M, Galvanetto U (2014) Crack propagation with adaptive grid refinement in 2D peri-

dynamics. Int J Fract 190:1–22. https://doi.org/10.1007/s10704-014-9970-4

Ferney BD, Devary MR, Hsia KJ, Needleman A (1999) Oscillatory crack growth in glass. Scr Mater 41:275–281. https://doi.org/10.1016/S1359-6462(99)00161-X

Ha YD, Bobaru F (2010) Studies of dynamic crack propagation and crack branching with peridynamics. Int J Fract 162:229–244. https://doi.org/10.1007/s10704-010-9442-4

Hayakawa Y (1994) Numerical study of oscillatory crack propagation through a two-dimensional crystal. Phys Rev E 49:1804–1807. https://doi.org/10.1103/PhysRevE.49.R1804

Hu W, Ha YD, Bobaru F, Silling SA (2012) The formulation and computation of the nonlocal J-integral in bond-based peridynamics. Int J Fract 176:195–206. https://doi.org/10.1007/s10704-012-9745-8

Hu W, Wang Y, Yu J et al (2013) Impact damage on a thin glass plate with a thin polycarbonate backing. Int J Impact Eng 62:152–165. https://doi.org/10.1016/j.ijimpeng.2013.07.001

Hussain AKMF (1986) Coherent structures and turbulence. J Fluid Mech 173:303. https://doi.org/10.1017/S0022112086001192

Kilic B, Madenci E (2009) Prediction of crack paths in a quenched glass plate by using peridynamic theory. Int J Fract 156:165–177. https://doi.org/10.1007/s10704-009-9355-2

Kilic B, Madenci E (2010) Peridynamic theory for thermomechanical analysis. IEEE Trans Adv Packag 33:97–105. https://doi.org/10.1109/TADVP.2009.2029079

Marder M (1994) Instability of a crack in a heated strip. Phys Rev E 49:51–55. https://doi.org/10.1103/PhysRevE.49.R51

Menouillard T, Belytschko T (2011) Analysis and computations of oscillating crack propagation in a heated strip. Int J Fract 167:57–70. https://doi.org/10.1007/s10704-010-9519-0

NVIDIA https://developer.nvidia.com/cublas

Pham VB, Bahr HA, Bahr U et al (2008) Global bifurcation criterion for oscillatory crack path instability. Phys Rev E Stat Nonlinear Soft Matter Phys 77:1–10. https://doi.org/10.1103/PhysRevE.77.066114

Ronsin O, Heslot F, Perrin B (1995) Experimental study of quasistatic brittle crack propagation. Phys Rev Lett 75:2352–2355. https://doi.org/10.1103/PhysRevLett.75.2352

Ronsin O, Perrin B (1998) Dynamics of quasistatic directional crack growth. Phys Rev E 58:7878–7886. https://doi.org/10.1103/PhysRevE.58.7878

Sakaue K, Yoneyama S, Kikuta H, Takashi M (2008) Evaluating crack tip stress field in a thin glass plate under thermal load. Eng Fract Mech 75:1015–1026. https://doi.org/10.1016/j.engfracmech.2007.04.025

Sakaue K, Yoneyama S, Takashi M (2009) Study on crack propagation behavior in a quenched glass plate. Eng Fract Mech 76:2011–2024. https://doi.org/10.1016/j.engfracmech.2009.05.008

Shewchuk JR (1994) An introduction to the conjugate gradient method without the agonizing pain. Technical Report CMUCS-TR-94-125, Carnegie Mellon University

Shilko EV, Psakhie SG (2014) Theoretical study of peculiarities of unstable longitudinal shear crack growth in sub-Rayleigh and supershear regimes. In: International conference on physical mesomechan, pp 571–574

Silling SA, Askari E (2005) A meshfree method based on the peridynamic model of solid mechanics. Comput Struct 83:1526–1535. https://doi.org/10.1016/j.compstruc.2004.11.026

Silling SA, Lehoucq RB (2010) Peridynamic theory of solid mechanics. In: Advances in applied mechanics, pp 73–168. https://doi.org/10.1016/S0065-2156(10)44002-8

Strogatz SH (2001) Nonlinear dynamics and chaos: with applications to physics, biology, chemistry and engineering. Westview Press, Boulder

Tian X, Du Q (2013) Analysis and comparison of different approximations to nonlocal diffusion and linear peridynamic equations. SIAM J Numer Anal 51:3458–3482. https://doi.org/10.1137/13091631X

van Wijk JJ (2002) Image based flow visualization. ACM Trans Graph 21:745–754. https://doi.org/10.1145/566654.566646

Yang B, Ravi-Chandar K (2001) Crack path instabilities in a quenched glass plate. J Mech Phys Solids 49:91–130. https://doi.org/10.1016/S0022-5096(00)00022-3

Yoneyama S, Sakaue K (2014) Experimental-numerical hybrid stress analysis for a curving crack in a thin glass plate under thermal load. Eng Fract Mech 131:514–524. https://doi.org/10.1016/j.engfracmech.2014.09.007

Yoneyama S, Sakaue K, Kikuta H, Takashi M (2008) Observation of stress field around an oscillating crack tip in a quenched thin glass plate. Exp Mech 48:367–374. https://doi.org/10.1007/s11340-007-9078-0

Yuse A, Sano M (1993) Transition between crack patterns in quenched glass plates. Nature 362:329–331. https://doi.org/10.1016/S0167-2789(97)00011-0

Yuse A, Sano M (1997) Instabilities of quasi-static crack patterns in quenched glass plates. Phys D Nonlinear Phenom 108:365–378. https://doi.org/10.1016/S0167-2789(97)00011-0

Zhang G, Le Q, Loghin A et al (2016) Validation of a peridynamic model for fatigue cracking. Eng Fract Mech 162:76–94. https://doi.org/10.1016/j.engfracmech.2016.05.008